

UV to near-IR observations of the DART-Dimorphos collision

Eran O. Ofek^{1*}, Doron Kushnir¹, David Polishook², Eli Waxman¹, Aaron Tohuvavohu³, Sagi Ben-Ami¹, Boaz Katz¹, Orly Gnat⁴, Nora L. Strotjohann¹, Enrico Segre², Arie Blumenzweig¹, Yahel Sofer-Rimalt¹, Ofer Yaron¹, Avishay Gal-Yam¹, Yossi Shvartzvald¹, Michael Engel¹, S. Bradley Cenko^{5,6}, Ofir Hershko²

¹*Department of Particle Physics and Astrophysics, Weizmann Institute of Science, 76100 Rehovot, Israel.*

²*Department of Physics Core Facilities, Weizmann Institute of Science, Herzl St 234, Rehovot 7610001, Israel*

³*Department of Astronomy and Astrophysics, University of Toronto, Toronto, ON, Canada*

⁴*Racah Institute of Physics, The Hebrew University, Jerusalem 91904, Israel*

⁵*Astrophysics Science Division, NASA Goddard Space Flight Center, MC 661, Greenbelt, MD 20771, USA*

⁶*Joint Space-Science Institute, University of Maryland, College Park, MD 20742, USA*

21 November 2023

ABSTRACT

The impact of the Double Asteroid Redirection Test (DART) spacecraft with Dimorphos allows us to study asteroid collision physics, including momentum transfer, the ejecta properties, and the visibility of such events in the Solar System. We report observations of the DART impact in the ultraviolet (UV), visible light, and near-infrared (IR) wavelengths. The observations support the existence of at least two separate components of the ejecta: a fast and a slow component. The fast-ejecta component is composed of a gaseous phase, moving at about 1.6 km s^{-1} with a mass of $\lesssim 10^4 \text{ kg}$. The fast ejecta is detected in the UV and visible light, but not in the near-IR z -band observations. Fitting a simplified optical thickness model to these observations allows us to constrain some of the properties of the fast ejecta, including its scattering efficiency and the opacity of the gas. The slow ejecta component is moving at typical velocities of up to about 10 m s^{-1} . It is composed of micrometer-size particles, that have a scattering efficiency, at the direction of the observer, of the order of 10^{-3} and a total mass of $\sim 10^6 \text{ kg}$. The larger particles in the slow ejecta, whose size is bound to be in the range between $\sim 1 \text{ mm}$ to $\sim 1 \text{ m}$, likely have a scattering efficiency larger than that of the pre-impact Didymos system.

Key words: minor planets: individual: Didymos — minor planets: individual: Dimorphos —

1 INTRODUCTION

The Double Asteroid Redirection Test (DART; Rivkin et al. 2021; Cheng et al. 2018) examined planetary defense strategies via the reaction of the near-Earth asteroid Dimorphos, a satellite of Didymos (65803), to a spacecraft impact (Daly et al. 2023; Cheng et al. 2023; Graykowski et al. 2023). The main goal of the DART mission was to measure the momentum gain due to the impact (Cheng et al. 2018; Cheng et al. 2023; Thomas et al. 2023; Gudebski et al. 2023). Indeed, measurements of the orbital period change (Thomas et al. 2023; Gudebski et al. 2023), of the Didymos-Dimorphos system, estimated the momentum gain by Dimorphos due to the DART impact to be about 4 (Cheng et al. 2023), which is consistent with the pre-impact predictions (e.g., 1–5; Fahnestock et al. 2022). DART observations already revealed several intriguing facts, including ejecta with a large spread of velocities, the presence of micro-

meter-sized particles as well as meter-size boulders in the ejecta, and a high-velocity gaseous phase in the ejecta (e.g., Shestakova et al. 2023; Roth et al. 2023; Moreno et al. 2023; Jewitt et al. 2023). Detailed observations of the velocity and particle-size distribution in the ejecta can be used to calibrate the models and assess the target properties (e.g., Housen et al. 1983; Fahnestock et al. 2022; Sánchez et al. 2022; Kumamoto et al. 2022).

Furthermore, the DART mission gives us some insight into the physics and visibility of asteroid collisions (e.g., Farinella & Davis 1992; Holsapple & Housen 2019; Holsapple 2022, Ofek et al., in prep.). Asteroid collisions were reported in the past (e.g., Jewitt et al. 2010, 2011; Haisch et al. 1991; Ishiguro et al. 2011; Moreno et al. 2011), but in all cases were likely detected many days or weeks after the impact. These collisions are also likely responsible for the production of some of the zodiacal dust (e.g., Gustafson 1994).

Here, we report on ultraviolet (UV), visible, and near-infrared (NIR) observations of the Dimorphos-DART impact. We show that the ejecta was composed of two main compo-

* E-mail: eran.ofek@weizmann.ac.il

Telescope	Filter	Observing window (2022 UTC)	Number of images
LAST	clear	09-26/27 23:12–02:38	2481
	clear	09-27/28 23:02–02:37	2350
	clear	09-28/29 22:30–02:30	2229
	clear	09-29/30 22:32–02:40	2474
	clear	10-01/02 22:12–01:47	1840
	clear	10-03/04 22:39–02:30	437
	clear	10-04/05 22:34–02:22	196
C28	<i>z</i>	09-26/27 23:00–02:30	645
UVOT	<i>UVW2</i>	09-26 23:08–23:20	Photon counting

Table 1. Summary of observations.

nents. A slow component expanding at a velocities of the order of a m s^{-1} and a fast component moving at $1,600 \text{ m s}^{-1}$. The brightening of the event after the collision is interpreted as a transition from an optically thick to an optically thin phase. This, as well as the surface brightness evolution, allows us to measure the scattering and opacity of the emitting gas in the fast ejecta. Furthermore, these observations may have implications for the visibility of asteroid collisions in the main belt, which in turn may be able to constrain the number of meter-sized asteroids (Ofek et al., in prep.).

The structure of this paper is as follows. In §2 we describe the observations, while in §3, we define the surface area units that we use, and in §4, we provide an overview of the ejecta. In §5, we discuss the fast-ejecta component, while in §6 the slow-ejecta component. Finally, we conclude in §7.

2 OBSERVATIONS

We obtained observations of the DART impact using the Large Array Survey Telescope (LAST; §2.1), the *Swift*-UVOT space telescope (§2.2) and the Rich 28-inch telescope (C28) at the Wise Observatory (§2.3). The Observations are summarized in Table 1. All the magnitudes in this paper are in the Vega system.

2.1 The Large Array Survey Telescope

The Large Array Survey Telescope (LAST) is an under-construction array of 48, 28-cm $f/2.2$ telescopes (Ofek & Ben-Ami 2020; Ben-Ami et al. 2023). At the time of DART impact, we used six out of 12 telescopes installed at that time¹. Each telescope provides a field of view of 7.4 deg^2 , and pixel scale of $1.25'' \text{ pix}^{-1}$. The LAST observations were taken without a filter. The LAST response is similar to that of the GAIA B_p band, but extending more into the red (from 4000 \AA to 8000 \AA and peaking at 4800 \AA), and it is calibrated to this band. During the impact, we observed with 5 s integrations and we switched to 20 s, after a few tens of minutes.

The LAST images were dark subtracted and flat corrected using tools available in the LAST data pipeline (Ofek 2023, 2014, 2019; Soumagnac & Ofek 2018). The code used for the

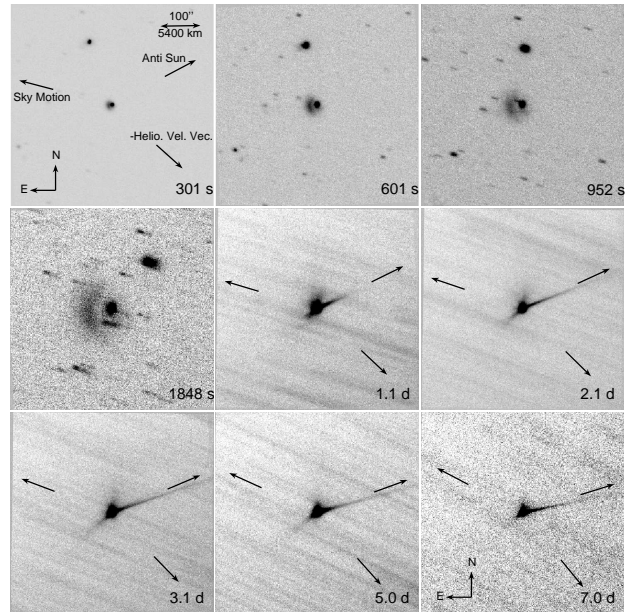


Figure 1. LAST B_p images of Didymos at selected times after the DART impact obtained by coadding (Zackay & Ofek 2017) a large number of images from different LAST telescopes. Also shown are the sky motion, antisolar direction, and the negative of the Heliocentric velocity vector of the asteroid.

data reduction is available online via GitHub². The Didymos light curve was obtained using a specialized version of the pipeline in which the photometry is performed on the predicted astrometric position of the asteroid. Given the extended nature of the target and the high airmass of observations, we have used several large photometric apertures of $5''$, $7.5''$, $10''$, and $12.5''$. The LAST photometry was calibrated against the B_p magnitude of a single GAIA star, on each night. To minimize the color term in the calibration, we choose stars with $B_p - R_p \approx 0.8$. In Table 2, we list all 12,007 photometric measurements collected by the LAST system. The B_p light curve of the event is shown in Figure 2, where the flux is presented in units of the effective surface area defined in §3.

The post-impact images of the Didymos system are shown in Figure 1. These images are based on the coaddition of multiple LAST images collected using several telescopes. The images were first registered to the predicted position of the Didymos asteroid, background subtracted, and flux matched (by the image photometric zero points), and then coadded using a median sigma-clipped coaddition. Table 3 summarizes the properties of the coadded images.

2.2 Swift-UVOT

We also observed the event using the *Swift*-UVOT (Gehrels et al. 2004; Roming et al. 2005), in event mode (11 ms time resolution) and the *UVW2* filter (1600 \AA to 3000 \AA and peaking at about 2000 \AA). The *Swift*-UVOT is

¹ Currently 32 telescopes are installed.

² <https://github.com/EranOfek/AstroPack>

JD (day)	Mag(5) (mag)	Mag(7.5) (mag)	Mag(10) (mag)	Mag(12.5) (mag)	Err(5) (mag)	Err(7.5) (mag)	Err(10) (mag)	Err(12.5) (mag)
2459849.4671696	14.674	14.701	14.669	14.723	0.026	0.025	0.024	0.024
2459849.4672276	14.706	14.741	14.743	14.779	0.026	0.025	0.025	0.025
2459849.4672855	14.581	14.676	14.719	14.807	0.025	0.025	0.025	0.026
2459849.4673433	14.695	14.712	14.741	14.667	0.026	0.025	0.025	0.024
2459849.4674013	14.608	14.573	14.538	14.465	0.025	0.023	0.022	0.021

Table 2. List of all 12,007 observations of the Didymos system collected using LAST. There are four magnitude and error columns corresponding to the aperture photometry around the predicted Didymos position in apertures with radii of $5''$, $7.5''$, $10''$, and $12.5''$. The full Table is available in the electronic version of this paper. Here we list the first five entries.

Mid time (s)	Time range (s)	Exposure time (s)
301.3	119.3	480
601.4	119.3	480
952.3	187.8	770
1849	372	1415
92268	12903	47260
177132	14389	43365
264763	14839	50140
434459	12876	36880
609478	13819	12900

Table 3. Properties of coadd images (Figure 2). Mid-time in seconds since impact, time range and total exposure time of all the coadded images.

a 30-cm telescope, with $0.5''/\text{pix}$, equipped with intensified CCD that can be operated in photon counting mode.

The *Swift* UVW2 observations, presented in Figure 2 and Table 4, detected Didymos prior to the impact at UVW2 Vega magnitude of 19.0 ± 0.1 . The UV excess flux peaked at $16.4_{-0.2}^{+0.3}$, about 35 s after the impact.

2.3 Wise 28-inch telescope

We observed using the Jay Baum Rich 28-inch (C28) telescope (Brosch et al. 2015) in the Wise Observatory, Mizpe-Ramon, Israel (about 65 km North of the LAST system). This telescope has a pixel scale of $0.83'' \text{ pix}^{-1}$. The C28 observations were conducted using a z -band filter (8100 \AA to 10000 \AA).

The C28 observations were calibrated against the SkyMapper catalog (Keller et al. 2007; Wolf et al. 2018). The pre-impact z -band magnitude of the system was 13.7 ± 0.2 (Vega) mag, and it peaked at about 12.4 mag, about 100 s after the impact. The 600 C28 observations, are listed in Table 5 and presented in Figure 2.

3 SURFACE AREA UNITS

We display the light curve of the DART impact using units of effective surface area (S_{eff}). The reason is that surface area units have a physical meaning relevant to reflection (the surface area of the reflecting particles) and to emission (the surface area is related to the mass of the particle via the opacity κ). For a geometry in which the dimensions of the scattering

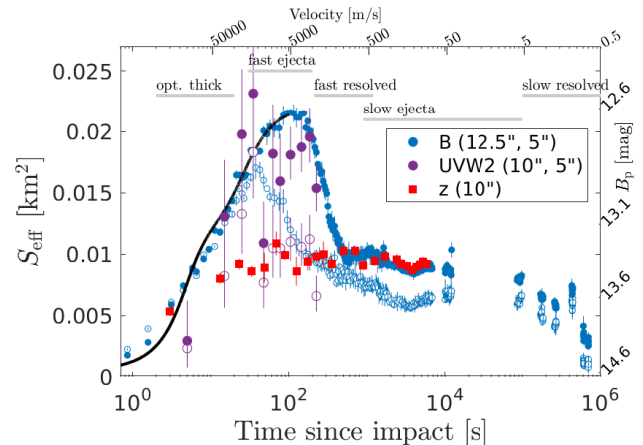


Figure 2. The Didymos system excess flux in units of effective area for scattering 100% of the solar radiation (§3). Time is measured relative to the light-time corrected impact time (0.2 s uncertainty; UTC 2022-09-26 23:15:01.9; LAST topocentric time). The filled (empty) purple points show the binned *Swift*-UVOT UVW2-band excess flux for a $10''$ ($5''$)-radius aperture, while the blue filled (empty) points show the binned B_p -band flux for $12.5''$ ($5''$)-radius apertures. The filled red boxes present the binned z -band light curve in the $10''$ -radius aperture. The corresponding B_p magnitude is shown on the right axis. The z -band magnitude can be obtained by subtracting 1 mag, while for the UVW2 add 4.5 mag. The top axis shows the velocity for which the ejecta would expand beyond the $10''$ aperture at that time. This velocity estimate is an approximation as it does not take into account the point spread function and ejecta geometry. The solid black curve shows the best fit (to the non-binned data) of our optical thickness model for the fast and slow ejecta (see also Figure 4). To mimic the 5 s exposures, the optical thickness model was convolved with a 5 s top-hat function. All error bars show $1-\sigma$ errors. The gray lines at the top show different phases of the light curve.

cloud in the radial and transverse directions is similar, we can write:

$$\kappa \sim \frac{S_{\text{eff}}}{M}, \quad (1)$$

where M is the mass of the ejecta. Here we define the effective surface area S_{eff} such that

$$f_x = f_{\odot,x} N_p \frac{d\sigma}{d\Omega}(\theta) \frac{1}{\Delta^2} \equiv f_{\odot,x} S_{\text{eff}} \frac{1}{\Delta^2}, \quad (2)$$

where f_x is the observed flux in band x , $f_{\odot,x} = L_{\odot,x}/(4\pi r^2)$ is the solar flux at band x , $L_{\odot,x}$ is the solar luminosity, r and Δ are the target Heliocentric and Geocentric distances,

Mid Time (s)	Mag(5) (mag)	Low Err(5) (mag)	High Err(5) (mag)	Mag(10) (mag)	Low Err(10) (mag)	High Err(10) (mag)
5.0	18.15	0.41	0.93	18.00	0.43	0.75
15.0	17.19	0.28	0.47	16.76	0.25	0.34
25.0	16.75	0.23	0.36	16.36	0.21	0.27
35.0	16.43	0.20	0.29	16.20	0.19	0.25
47.5	17.25	0.24	0.37	16.93	0.22	0.29
62.5	16.97	0.21	0.31	16.44	0.18	0.22
77.5	16.97	0.21	0.31	16.57	0.19	0.24
105.0	16.92	0.13	0.17	16.44	0.11	0.13
145.0	16.96	0.13	0.17	16.41	0.11	0.12
185.0	16.91	0.13	0.16	16.37	0.11	0.12
225.0	17.38	0.16	0.21	16.61	0.12	0.14

Table 4. Summary of *Swift*-UVOT observations. The observations were obtained using the *UVW2* filter in photon counting mode, and the number of photons in each time bin was converted to Vega magnitudes. The errors were calculated assuming Poisson statistics (Gehrels 1986). The flux was converted to magnitudes using the instrument zero point. The time is measured relative to the light-travel time corrected impact time. The bin sizes are adaptive. The first bin starts in 0 seconds, and the mid-time indicates the middle of each time bin. The measurements are based on aperture photometry with 5'' and 10'' aperture radii. The pre-impact magnitude of the Didymos system was 19.04.

Time (s)	Mag (mag)	Err (mag)
-1778.5	14.02	0.43
-1768.3	13.97	0.27
-1758.2	13.19	0.21
-1748.0	13.53	0.30
-1737.9	13.03	0.15

Table 5. Summary of the C28 observations. The observations were obtained using the *z* filter. The measurements are based on aperture photometry with 10'' aperture radius. We list here the first five measurements, while the full Table is available with the electronic version of this manuscript.

respectively, N_p is the number of particles and $d\sigma/d\Omega(\theta)$ is the cross section for scattering at angle θ (with units of sr^{-1}).

Using the definition for S_{eff} , its relation to magnitude in band x is given by:

$$S_{\text{eff,tot}} = 10^{0.4(M_{\odot,x} - M_x) + 2 \log_{10}(r\Delta)}, \quad (3)$$

where M_x is the apparent magnitude of the asteroid and $M_{\odot,x}$ is the Geocentric apparent magnitude of the Sun, in band x . For r and Δ in AU, S is in AU^2 . To derive the excess surface area of the ejecta, we subtract the Didymos surface area as calculated from the pre-impact magnitude of Didymos ($M_{\text{pre},x}$):

$$S_{\text{eff}} = S_{\text{eff,tot}}(M_x) - S_{\text{eff,tot}}(M_{\text{pre},x}). \quad (4)$$

4 OVERVIEW DESCRIPTION OF THE LIGHT CURVE

Following the DART impact, we observe two main resolved ejecta components. On time scales of the order of ten minutes after the impact, a spherical-cup-like component is detected moving eastward. This component has an opening angle of about two radians. We refer to this component as the *fast ejecta*. This ejecta is seen up to about one hour after the impact, when its surface brightness drops below our detection

limit (see Figure 1, 5). After about a day, we resolve another, seemingly distinct, part of the ejecta we refer to as the *slow ejecta*. This component is composed of a fan line component and a tail (see also, e.g., Daly et al. 2023; Li et al. 2023; Roth et al. 2023; Moreno et al. 2023). Spectroscopic observations of the fast ejecta (Shestakova et al. 2023) showed that a major part of the light of this component arrives from emission lines of neutral species (Na I λ 5890, 5896 Å, K I λ 7699 Å, Li I λ 6708 Å), suggesting that the DART impact released gas. The origin of this gas is unknown but could be either a trapped gas or a gas created by the impact itself. For example, energy conservation does not prohibit the creation of a gaseous phase. Specifically, by equating the kinetic energy to the thermal energy, we can get an upper limit on the temperature of the heated material in the impact:

$$T \lesssim \frac{m_A v_{\text{imp}}^2}{k_B}. \quad (5)$$

Here m_A is the atom mass, $v_{\text{imp}} \cong 6,145 \text{ m s}^{-1}$ (Cheng et al. 2023) is the impact velocity, and k_B is the Boltzmann constant. For Sodium atoms, this provides an upper limit of about 10^5 K . However, this is likely limited to a small fraction of the ejecta. Interestingly, such intermittent Sodium emission was also detected in other Solar System objects like Phaethon (3200) and Mercury (e.g., Lierle et al. 2023; Zhang et al. 2023).

It is known that neutral species can not survive for long periods of time in the radiation field of the Sun. For example, Shestakova et al. (2023) estimate that at distance of 1 AU from the Sun, Na I and K I will become ionized on time scale of 1 day, while Li I will become ionized within about 1 hr. Therefore, given that the fast-ejecta visible light is dominated by Na I and K I emission lines, we estimate that during our fast-ejecta observations, the emission lines' luminosity does not change considerably. This assumption is roughly confirmed by the measurement of the surface brightness evolution (§5.2).

Following the impact, the light curve rises in all bands within 100 s. We attribute this rise to an optical thickness effect, *i.e.*, at early times, when the density of the ejecta is high enough, some of the gas or dust (depending on the com-

ponent) is being self-obscured. In Appendix A, we derive a simplified model for the optical thickness of the ejecta. Following the rise, the UV and blue optical observations show a peak lasting for about 100 s followed by a drop to an intermediate level. The first drop in the light curve is attributed to the fast ejecta leaving the photometric aperture. Indeed, the peak of the light curve, as detected in the larger photometric aperture, lasts longer than the peak at the smaller photometric apertures. Contrary to the UV and visible light, the z -band observations rise, but directly to the intermediate level. This suggests that there are no prominent emission lines in the z band (in the range of 8100 Å to 10000 Å). About one day after the impact, the light curve starts to drop, on a time scale of about one week, from its intermediate level back to the pre-impact luminosity. This second drop is due to the slow ejecta leaving the photometric aperture.

Finally, at later times, solar radiation sorts the ejecta particles by size, where micro-meter size particles form a tail.

5 THE FAST EJECTA

To measure the velocity of the fast ejecta, we linearly fitted the time-dependent angular distance between the asteroid and the brightest pixel in the fast ejecta, convolved with the point spread function (PSF) – i.e., a matched filter detection. Next, we converted this angular speed to velocity, using the known distance to the Didymos system. The fast ejecta position angle of motion is 108 deg, and its projected speed is $v_{\text{ej,fast}} = 1.6 \pm 0.2 \text{ km s}^{-1}$. Since the expected direction of the impact, and hence the ejecta, is about 90 deg from the observer-Dimorphos line (e.g., Rivkin et al. 2021), this measured velocity is likely close to the actual ejecta velocity. The largest uncertainty in the velocity is due to the on-sky projection angle, which here we assume is known to about 10% accuracy. This estimate is consistent with the fast ejecta velocity measured by Shestakova et al. (2023). However, it differs from the value given in Graykowski et al. (2023) (of $970 \pm 50 \text{ m s}^{-1}$). These authors estimate the velocity from the light curve – i.e., from the time it takes the ejecta light to get out of the photometric aperture. However, such an estimate depends on the exact ejecta geometry and seeing.

We can use this velocity, along with energy conservation, to put an upper limit of the mass of the fast ejecta:

$$m_{\text{ej,fast}} \lesssim m_{\text{imp}} \left(\frac{v_{\text{imp}}}{v_{\text{ej,fast}}} \right)^2. \quad (6)$$

Here, $m_{\text{imp}} = 579.4 \text{ kg}$ is the impactor mass, and $v_{\text{imp}} = 6.145 \text{ km s}^{-1}$ is the impactor velocity (Cheng et al. 2023). This translates to an upper limit of $m_{\text{ej,fast}} \lesssim 10^4 \text{ kg}$. We note that if the mass of the fast ejecta is close to this limit, then the measured momentum gain of the impact (Cheng et al. 2023) is dominated by this fast ejecta. However, estimating the mass of the fast ejecta requires a non-steady-state radiative model.

We estimate the effective area, defined in §3, of the fast-ejecta component, by reading the total surface area of the peak in Figure 2 and subtracting the surface area of the plateau region (slow ejecta, at around an hour after the impact). We find that the effective surface area of the fast ejecta is about 0.0125 km^2 . This value suffers from several uncertainties that are not straightforward to estimate, including

what is the fraction of slow-ejecta surface brightness during the fast-ejecta peak, which is still optically thick, and the existence of additional ejecta components. This estimate is also consistent with a direct measurement of the total flux of the resolved fast ejecta we obtained by integrating the light of the fast ejecta in the LAST images taken about 30 min after the impact. The effective surface area (or flux) ratio of the fast-ejecta component between the different bands (UV , B_p and z) are: $0.3 < S_{\text{eff,fast,UV}}/S_{\text{eff,fast,B}} < 3$, and $S_{\text{eff,fast,B}}/S_{\text{eff,fast,z}} > 4$.

We note that prior to the finding that the fast-ejecta light is mainly due to emission lines (Shestakova et al. 2023), we interpreted these observations as Mie-scattering on sub-micron particles. Such a model allows the estimation of the fast-ejecta mass (including the absorbing/unseen particles) and even the dielectric properties of the particles. However, given the observations of emission lines, this interpretation can be ruled out (see Appendix B).

Finally, using Equation 1, and the upper limit on the mass of the fast ejecta, we can put a lower limit on the gas effective opacity, of $\kappa \gtrsim 10^4 \text{ cm}^2 \text{ g}^{-1}$.

5.1 The rising light curve

We interpret the rise of the light curve as a transition from an optically thick to an optically thin phase. Evidence for the correctness of this interpretation was seen directly in the case of the *DeepImpact* collision with Temple 1 where the shadow of the ejecta is directly seen (A’Hearn et al. 2005; Harker et al. 2005; Meech et al. 2005).

In Appendix A, we derive a simplified model for the optical thickness as a function of time, as well as the surface brightness of the event. This model assumes a single scattering of photons before they escape from the ejecta (i.e., the cross-section for absorption is larger than the cross-section for scattering). For line emission, this means that a UV photon is not exciting more than one atom. In this Appendix, we also discuss the caveats in this model. The ejecta geometry is assumed to be a spherical shell section with a half-opening angle γ , and a width over distance ratio of δ . The time scale for the optically thick to optically thin transition is

$$t_0 = \sqrt{\frac{9m_{\text{ej}}\sigma_{\text{T}}}{8\pi^2\rho r_{\text{p}}^3 v_{\text{ej}}^2 (1 - \cos(\gamma))}}. \quad (7)$$

Here σ_{T} is the total (absorption and scattering) cross-section of each particle, ρ is the particle density, and r_{p} is its radius. For gas, one can replace ρ and r_{p} with the particle mass (i.e., $m_{\text{p}} = (4/3)\rho r_{\text{p}}^3$).

We fitted the first 100 s after impact, of the Didymos B_p light curve with the spherical cup optical thickness model. We use data obtained in the $12.5''$ -radius aperture, and we assumed $S_{\text{fast,B}} = 0.0125 \text{ km}^2$, $\gamma_{\text{fast}} = 1$, and $\delta_{\text{fast}} = 0.5$ for the fast ejecta, and $S_{\text{slow,B}} = 0.0095 \text{ km}^2$, $\gamma_{\text{slow}} = \pi/2$, and $\delta_{\text{slow}} = 1$ for the slow ejecta. In order to calculate the χ^2 between the observations and the model, we convolved the model with a top-hat function with 5 s width (to mimic the 5 s exposure time). This allows us to probe t_0 , which is shorter than our time resolution. The χ^2 as a function of $t_{0,\text{fast}}$ and $t_{0,\text{slow}}$ is presented in Figure 3. The contours show the 1, 2, and 3- σ confidence levels. To show the sensitivity to other values of γ and δ we also show (in dashed contours) the χ^2

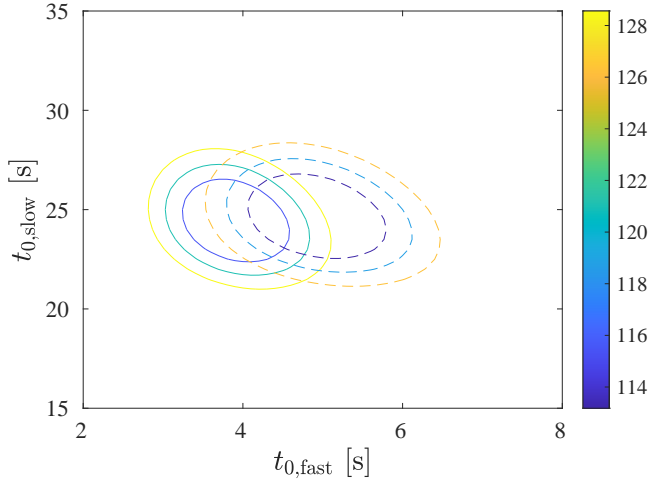


Figure 3. The χ^2 surface of the best fit $t_{0,\text{fast}}$ and $t_{0,\text{slow}}$ to the rising light curve (first 100 s). The solid contours are for fast ejecta with $\gamma_{\text{fast}} = 1$, $\delta_{\text{fast}} = 0.5$, and slow ejecta with $\gamma_{\text{slow}} = \pi/2$, $\delta_{\text{slow}} = 1$, while the dashed contours are for fast ejecta with $\gamma_{\text{fast}} = 1$, $\delta_{\text{fast}} = 0.2$, and slow ejecta with $\gamma_{\text{slow}} = 1.5$, $\delta_{\text{slow}} = 1$.

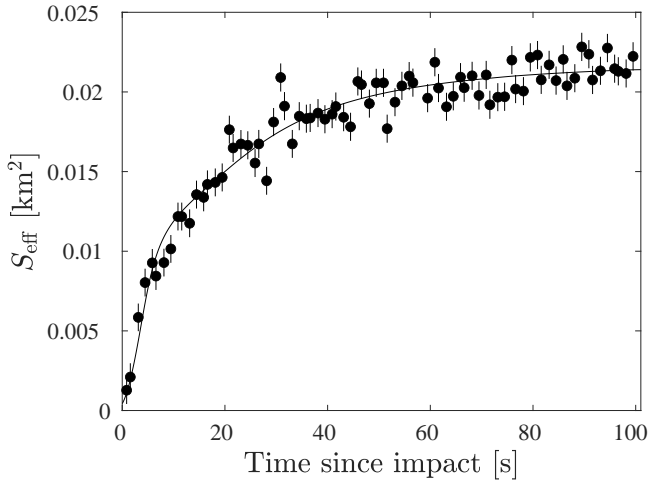


Figure 4. The rising (unbinned) light curve (first 100 s) obtained using LAST in the B_p band and photometric aperture radius of $12.5''$. Errors represent $1\text{-}\sigma$ uncertainties. The black line shows the best-fit rise model using $t_{0,\text{fast}} = 3.9\text{ s}$ and $t_{0,\text{slow}} = 24.5\text{ s}$.

contours for $\gamma_{\text{fast}} = 1$ and $\delta_{\text{fast}} = 0.2$ for the fast ejecta, and $\gamma_{\text{slow}} = 1.5$ and $\delta_{\text{slow}} = 1$ for the slow ejecta. We get best fit values of $t_{0,\text{fast}} = 3.9 \pm 0.5\text{ s}$ and $t_{0,\text{slow}} = 24.5 \pm 2\text{ s}$ (with best fit $\chi^2/\text{dof} = 108/92$). The errors were calculated assuming six degrees of freedom (to mimic all the free parameters in the problem).

5.2 Surface brightness evolution

For constant emission or reflection from particles expanding at a constant velocity, the surface brightness evolves like t^{-2} . Therefore, by measuring the surface brightness of the fast ejecta, we can extrapolate its brightness at early times and find the surface brightness at which the fast ejecta becomes optically thin (i.e., $t_{0,\text{fast}} \approx 3.9\text{ s}$). This surface brightness is equivalent to the efficiency in which UV Sunlight excites

the atoms that emit their light in the visible band. I.e., the scattering efficiency ($d\sigma/d\Omega(\theta)/\sigma_T$) of the fast ejecta. Here $d\sigma/d\Omega(\theta)$ is the cross section for scattering at direction θ (53.3 deg in our case), and σ_T is the total cross section for absorption and scattering.

We measure the maximum surface brightness as a function of time along the line connecting Didymos with the fast ejecta trajectory (i.e., position angle of 108 deg). After converting these flux measurements to surface brightness, this provides a measurement of $I_{x,\text{max}}$ (the maximum surface brightness, defined in §A). Assuming $\gamma = 1$ and $\delta = 0.5$, the ratio between the maximum surface brightness and the mean surface brightness is about 1.92 (derived in §A2).

In Figure 5, we show the surface brightness (in magnitude per arcsec²) as a function of time. The red points show the measured surface brightness from the resolved ejecta. The power-law index of the red points deviates from 2 because, presumably, at early times, given our poor spatial resolution, the fast ejecta is not fully resolved (in the motion direction). Therefore, when extrapolating the surface brightness to early times (black line) we anchor the extrapolated line to the latest measurements at $t \approx 1000\text{ s}$. The black dots show our early $12.5''$ -radius aperture photometry converted to surface brightness by extrapolating the area of the ejecta by $(v_{\text{ej}}(t + dt))^2$. Since at the first few seconds, the flux evolves like t^2 , we added dt , which is $1/4$ of the exposure time. The blue line shows the best fit optical thickness model for the fast ejecta component (fitted in §5.1 and shown in Figure 4), converted to surface brightness. At late times, the black dots are above the blue line because they include the slow ejecta. The best fit $t_{0,\text{fast}}$ is marked as a vertical dotted line, and this line intersects the black solid line at a level of $d\sigma/d\Omega(\theta)/\sigma_T \approx 3 \times 10^{-4}$.

6 THE SLOW EJECTA

6.1 The slow ejecta particle size and scattering properties

We detect a slow ejecta component composed of a tail and fan-like structure (see also Li et al. 2023; Moreno et al. 2023). This component is responsible for the second plateau in the light curve, which started about 600–1000 s after the impact and extends up to about 1 day. From its brightness we get $S_{\text{ej,slow,B}} \approx 0.0095\text{ km}^2$. From the fact that the second plateau started declining at $t \sim 1\text{ day}$, and reached an effective surface area of 0.002 km^2 by day 8, we can estimate that the slowly-moving ejecta had typical projected velocities in the range of ~ 0.5 to $\sim 10\text{ m s}^{-1}$, with roughly half the surface area with a projected velocity below $\sim 4\text{ m s}^{-1}$. Since this velocity is estimated using the time it takes the flux to leave the photometric aperture, we estimate it may suffer from a factor of 2 uncertainty.

The time scale on which the ejecta become optically thin (i.e., t_0) is consistent with the fact that the maximum surface area in the larger photometric apertures is bigger than the one in the smaller apertures and converges for an aperture radius of about $10''$. Specifically, for $t_{0,\text{slow}} \approx 25\text{ s}$ (see Appendix A), the slow ejecta light curve is still not fully optically thin at 100 s after the impact. Therefore, the flux in the larger aperture increases as the slow ejecta becomes optically

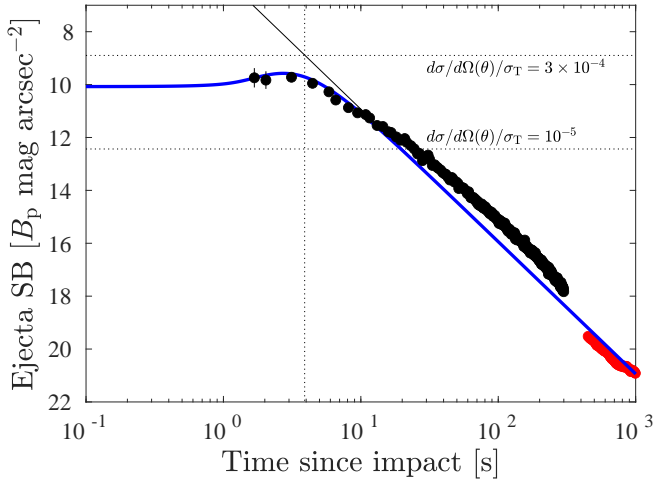


Figure 5. The measured B_p surface brightness [magnitude arcsec $^{-2}$] of the brightest pixel in the fast ejecta (along the motion direction) as a function of time (red circles). The black circles show the surface brightness as estimated from the photometry divided by $(v_{\text{ej,fast}}t)^2$, while the blue line shows the corresponding optical thickness model (see text for details). The errors of the black dots include the propagated uncertainty due to the pre-impact magnitude of the system and the uncertainty at the time of impact. The vertical dotted line shows the optical thickness time scale of the fast ejecta (i.e., $t_0 = 3.9$ s). The vertical dotted line crosses the surface brightness extrapolation (black line) at $d\sigma/d\Omega(\theta)/\sigma_T = 2.6 \times 10^{-4}$. The dotted horizontal lines show the surface brightness levels for $d\sigma/d\Omega(\theta)/\sigma_T$ of 10^{-5} , and 2.6×10^{-4} .

thin, while the flux in the smaller aperture decreases as the fast ejecta leaves the aperture.

Assuming a projected velocity with a flat distribution between 0.5 and 10 m s^{-1} , $\sqrt{\langle v_{\text{ej,slow}}^2 \rangle} \gtrsim 6 \text{ m s}^{-1}$, and from the kinetic energy conservation (Eq. 6), we can put an upper limit on the mass of the slow ejecta $\lesssim 6 \times 10^8 \text{ kg}$ (about 10% of Dimorphos mass). This limit is independent of the scattering properties of the ejecta. Using this upper limit, along with the ratio between surface area and mass we can put an upper limit on the average particle radius:

$$\begin{aligned} \tilde{r}_{\text{p,slow}} &\approx \frac{3m_{\text{ej}}}{4\rho S_{\text{eff}}} \frac{d\sigma/d\Omega(\theta)}{\pi\tilde{r}_{\text{p}}^2} \\ &\lesssim 14 \left(\frac{\rho}{3500 \text{ kg m}^{-3}} \right)^{-1} Q_{\text{scat}}(\theta) \text{ m}, \end{aligned} \quad (8)$$

where $Q_{\text{scat}}(\theta) = d\sigma/d\Omega(\theta)/(\pi r_{\text{p}}^2)$, and $\theta = 53.3$ deg (i.e., the scattering cross section in units of the geometric cross-section), r_{p} is the scattering particle radius, and ρ is the particle density. For the slow ejecta, we adopted $\rho = 3500 \text{ kg m}^{-3}$ consistent with stony meteorites (Britt & Consolmagno 2003). If the slow ejecta material is similar in scattering properties to the asteroid's surface material, then its scattering efficiency, as measured from the pre-impact light, is about 0.008, and hence $\tilde{r}_{\text{p,slow}} \lesssim 0.11 \text{ m}$. In HST images obtained months after the impact Jewitt et al. (2023) found dozens of slowly moving ($\sim 0.3 \text{ m s}^{-1}$) point sources around Didymos. Assuming they have the albedo of Didymos, their size is about 3 m. Since our upper limit on the particle size refers to the (reflected light-weighted) av-

erage particle size in the slow ejecta and not to the largest particles, our limit is consistent with their results.

Another limit on the particle size in the ejecta can be obtained from the smoothness of the ejecta. Since the slow ejecta in the images look smooth (i.e., we do not see discrete particles) we get, for mono-size particles, $r_{\text{p}} \lesssim (S/[\pi N_{\text{p,slow}}])^{1/2}$, where $N_{\text{p,slow}}$ is the number of discrete particles in the slow ejecta. For $N_{\text{p,slow}} \gtrsim 1000$, we get $r_{\text{p,slow}} \lesssim 20 \text{ m}$. However, the direct detection of meter-size particles by Jewitt et al. (2010) supersedes this estimate.

By substituting Equation 8 and the Equation for the optical thickness time scale t_0 (Appendix A; Equation A14) and rearranging we get

$$\frac{d\sigma/d\Omega(\theta)}{\sigma_T} \sim \frac{3}{2\pi} \frac{S_{\text{eff}}}{v_{\text{ej}}^2 t_0^2 (1 - \cos \gamma)} \quad (9)$$

Here σ_T is the total cross-section for absorption and scattering (see Appendix A). This equation provides an estimate of the scattering properties of the slow ejecta. Given an upper limit on the slow-ejecta velocity, this can be used to set a lower limit on the scattering efficiency of the mm-size (and above) particles in the slow ejecta (assuming $\gamma \sim 1$):

$$\frac{d\sigma/d\Omega(\theta)}{\sigma_T} \gtrsim 0.07 \frac{S_{\text{eff}}}{0.0095 \text{ km}^2} \left(\frac{v_{\text{ej}}}{10 \text{ m s}^{-1}} \frac{t_0}{24.5 \text{ s}} \right)^{-2} \quad (10)$$

However, due to projection effects, the actual velocity may be somewhat larger than 10 m s^{-1} . Nevertheless, this suggests that the large particles in the slow ejecta have scattering efficiency, which is at least a factor of a few larger compared to the pre-impact scattering efficiency of Didymos. Interestingly Polishook et al. (2023) found that the spectral slope of the IR spectra of the slow ejecta component is bluer compared to the pre-impact spectra of Didymos.

6.2 Tail and radiation pressure

About 24 hr after the impact, a thin tail appeared at a position angle of about 289 deg (see also Li et al. 2023; Moreno et al. 2023). The position angle of the antisolar vector (at day 3 from impact) is 293 deg, and the position angle of the negative of the Heliocentric velocity vector is 224 deg. On day two, the tail extends over 200 arcsec. Assuming the tail is in the antisolar direction and given that the Sun-Didymos-Earth angle is 60 deg, this is translated to tail length of $l_{\text{tail}} \approx 1.2 \times 10^7 \text{ m}$. The particles in the tail are presumably accelerated by solar radiation pressure. For spherical particles, this acceleration is given by

$$a_{\text{R}} \approx \frac{\pi r_{\text{p}}^2}{4/3\pi\rho r_{\text{p}}^3} \frac{L_{\odot}}{4\pi r^2 c} = \frac{3L_{\odot}}{16\pi\rho c r_{\text{p}}^2}, \quad (11)$$

where L_{\odot} is the Sun luminosity, and c is the speed of light. The maximum acceleration is $\approx 2l_{\text{tail}}/t^2 \sim 3 \times 10^{-4} \text{ m s}^{-2}$. Assuming the particles in the tail have Regolith-like densities (McKay et al. 1972) of about $1,500 \text{ kg m}^{-3}$, and combining this with the measured maximum acceleration indicates particles at the edge of the tail have a radius of about $7 \mu\text{m}$, with closer-to-Dimorphos parts of the tail containing bigger particles ($\sim 0.1 \text{ mm}$). This is consistent with the findings of Moreno et al. (2023). We note that in such cases, infrared spectroscopy or photometry of the tail may reveal, via Mie scattering analysis (see Appendix B), the size distribution and dielectric properties of the particles. This is crucial for

estimating the mass of the dust particles, as the actual scattering properties of the particles may differ significantly from assumptions based on the global albedo of the asteroid (see, e.g., Figure B1).

We measure the surface brightness of the tail as a function of distance from Didymos, and its integrated brightness, from $16''$ to $200''$ amounts to $S_{\text{tail}} \approx 8 \times 10^{-3} \text{ km}^2$. Using Equation 8, with the particle radius and surface brightness as a function of distance from Didymos, we estimate the mass of the tail as a function of distance. The integrated mass of the tail amounts to $m_{\text{tail}} \sim 800 Q_{\text{scat,tail}}^{-1}(\theta) \text{ kg}$, with $\theta = 53.3 \text{ deg}$, independent of the particle density. Assuming Mie scattering with $n + i\kappa = 1.5 + 0.3i$ (appropriate for Silica dust; [Draine & Lee 1984](#)) and $\sim 10 \mu\text{m}$ particles, $Q_{\text{scat}}(\theta) \sim 10^{-3} \text{ sr}^{-1}$ with weak dependency on the particle size (see Fig. B1), the mass of the tail is $m_{\text{tail}} \sim 8 \times 10^5 \text{ kg}$.

The fact that the tail is narrow suggests that the spread in the initial velocity of the particles in the tail is smaller than 0.3 m s^{-1} (i.e., spreading by less than $1''$ over four days). This velocity is comparable to the escape velocity from the Didymos system at the Dimorphos orbit.

Material ejected in such low velocities will become optically thin (Equation A14 with $\gamma = 1$) at around

$$t_0 \approx 10^4 \left(\frac{m_{\text{ej}}}{8 \times 10^5 \text{ kg}} \frac{\rho}{1.5 \text{ g cm}^{-3}} \right)^{1/2} \left(\frac{\tilde{r}_{\text{p}}}{20 \mu\text{m}} \right)^{-1/2} \left(\frac{v_{\text{ej}}}{0.3 \text{ m s}^{-1}} \right)^{-1} \quad (12)$$

where we normalize the density to the regolith density ([McKay et al. 1972](#)), and we use an average particle radius of $20 \mu\text{m}$. Interestingly, at times between 1000 s to about 10^4 s the light curve rises by (at least) $\sim 0.001 \text{ km}^2$ (~ 0.05 -magnitudes wiggle in Fig. 2). Although the observations were obtained at high airmass (in the range of 2.2 to 3.8), the fact that they are seen in both the C28 and LAST data sets, and the telescopes are separated by about 65 km , which likely means that the variations are real. Assuming that the wiggle in the light curve at 10^4 s corresponds to $t_0 \sim 3000 \text{ s}$ and that the ejection velocity of the tail particles is between 0.1 to 0.3 m s^{-1} , using Equation 9 we get $Q \sim 10^{-3}$. This is consistent with the expected scattering efficiency of μm -size Silica dust particles ([Draine & Lee 1984](#); see Fig. B1).

The tail appears about 4 deg off the antisolar direction towards the negative of the heliocentric velocity vector. This is presumably due to the Coriolis force that acts on the tail particles in the non-inertial frame of the asteroid. The Coriolis force acts in the direction of the negative of the Heliocentric velocity vector of the asteroid, where its expected acceleration, in this direction, is $a_{\text{C}} = 2\omega a_{\text{R}} t$, where $\omega \approx 2 \times 10^{-7} \text{ rad s}^{-1}$ is the angular velocity of the asteroid around the Sun, and the expected (non-projected) angle of the tail from the antisolar direction towards the negative of the Heliocentric velocity vector is

$$\tan \xi \approx \frac{a_{\text{C}} t^2 / 2}{a_{\text{R}} t^2 / 2} = \frac{\omega a_{\text{R}} t^3}{a_{\text{R}} t^2 / 2} = 2\omega t. \quad (13)$$

This approximation is valid because the tail length is much smaller than the orbital size. Since the tail is short we can neglect additional forces (e.g., Lorentz force and Poynting-Robertson drag). Since the angle between the observer and target orbital plane, measured from the center of the target was 49 deg (at $t = 3 \text{ day}$), then the expected tilt is $\xi \sin(49 \text{ deg}) \cong 4.8 \text{ deg}$, close to the observed angle of the

tail. At later times there is some evidence that the deviation is larger. This may be related to the double tail reported in the *HST* images of the impact (e.g., [Li et al. 2023](#); [Kim & Jewitt 2023](#); [Moreno et al. 2023](#)).

There are two possible explanations for the double-tail appearance. [Kim & Jewitt \(2023\)](#) show that such a structure can be formed by the spread in the directions in which the tail's material is ejected. An alternative explanation is due to an ejection of material at later times (a few days after the impact). Such a model was suggested by [Tancredi et al. \(2022\)](#). Interestingly, the light curve of the DART impact (Fig. 2) shows a brightening on day four after the impact, which can be consistent with such a late time ejection.

Next, the bulk of the resolved slow ejecta does not drift in the antisolar direction, and, therefore, is not strongly affected by the solar radiation pressure. This can be used to put a lower limit on the particle size (see also [Li et al. 2023](#); [Moreno et al. 2023](#)). The images suggest that, around day 3–5, the curvature of the fans toward the antisolar direction is smaller than $\mathcal{C} < 1/10$. Therefore, the particle acceleration due to the solar radiation pressure is: $a_{\text{R,fans}} \lesssim 2v/(\mathcal{C}t)$. For $v = 4 \text{ m s}^{-1}$ and $t = 5 \text{ day}$ we get $a_{\text{R,fan}} \lesssim 2 \times 10^{-6} \text{ m s}^{-2}$, which in turn, using Equation 11, gives $r_{\text{p,slow}} \gtrsim 0.4 \text{ mm}$. Substituting into Equation 8, we can put a lower limit on the mass of the slow ejecta: $m_{\text{ej,slow}} \gtrsim 1.8 \times 10^5 Q_{\text{scat}}^{-1}(\theta) \text{ kg}$. Assuming $Q_{\text{scat}} \sim 0.07$, the mass of the slow ejecta is $m_{\text{ej,slow}} \gtrsim 3 \times 10^6 \text{ kg}$. Furthermore, assuming the process responsible for the slow ejecta also created a crater whose depth-to-radius ratio is d , then the crater radius (from simple geometric considerations) is

$$r_{\text{crater}} \sim \left(\frac{m_{\text{ej}}}{\pi \rho d} \right)^{1/3}, \quad (14)$$

and with $d = 1/3$, we get a lower limit of $r_{\text{crater}} \gtrsim 9 \text{ m}$.

7 CONCLUSIONS

We present UV, visible light, and near-IR (z -band) observations of the DART impact ([Rivkin et al. 2021](#)). We use these observations to estimate the properties of the ejecta, which are summarized in Table 6. The observations suggest that the ejecta is composed of two main velocity components. A fast component that contains gas ([Shestakova et al. 2023](#)), and a slow component. The two components seem to be well separated in velocity, and they seem to have different geometric appearances. The slow ejecta contains both micro-meter size particles (that form the tail), as well as mm-sized (and larger, up to a few meters) particles that are only weakly affected by the solar radiation pressure. Although some simulations predict that the highest velocities of the ejecta will be of the order of 2 km s^{-1} ([Luther et al. 2018](#)), close to the observed value, as far as we know, these simulations do not predict an ejecta with bimodal velocity distribution.

An interesting question is which velocity component dominates the momentum transfer gained by the impact. Following [Cheng et al. \(2023\)](#) we define the momentum gain by:

$$\beta = 1 + \frac{M\Delta\vec{v} - m_{\text{imp}}\vec{v}_{\text{imp}}}{m_{\text{imp}}(\hat{E} \cdot \vec{v}_{\text{imp}})\hat{E}} \approx 1 + \frac{P_{\text{ej}}}{m_{\text{imp}}v_{\text{imp}}}. \quad (15)$$

Here, $M\Delta\vec{v}$ is the momentum change of Dimorphos due to

the impact, \hat{E} is the net ejecta momentum direction, and P_{ej} is the ejecta momentum. The left equality is the β definition used by the DART team (Cheng et al. 2023), while the right-hand side approximation is written in terms of the ejecta mass and velocity, which are measured in this work. Given the observed momentum gain ($\beta \sim 4$; Cheng et al. 2023), and the approximate velocity of the slow ejecta ($\sim 4 \text{ m s}^{-1}$), a slow-ejecta mass of the order of $\sim 3 \times 10^6 (v_{\text{ej,slow}}/4 \text{ m s}^{-1})^{-1} \text{ kg}$ is needed in order to explain the observed value of $\beta \sim 4$. This is consistent with the limits we find. We note that Kim & Jewitt (2023) estimated the total mass of the slow ejecta to be $\sim 2 \times 10^7 \text{ kg}$ (Didymos albedo was assumed). This estimate suggests that the slow ejecta dominates the momentum gain of the impact. On the other hand, if the fast-ejecta dominated the momentum-transfer gain, then a fast-ejecta mass of the order of $7 \times 10^3 \text{ kg}$ is required. A possible way to solve the question of which ejecta component dominated the momentum-transfer gain, is to better estimate the fast-ejecta mass. This may be possible by a non-steady state modeling of the radiative processes of the fast-ejecta gas.

ACKNOWLEDGEMENTS

We are thankful to the staff of the Tel-Aviv University Wise Observatory; Didymos is the first target simultaneously observed by the LAST array at the Weizmann Astrophysical Observatory and telescopes at the Wise Observatory. E.O.O. is grateful for the support of grants from the Benozziyo Center, Willner Family Leadership Institute, Ilan Gluzman (Secaucus NJ), Madame Olga Klein - Astrachan, Minerva Foundation, Israel Science Foundation, BSF-NSF, Israel Ministry of Science, Weizmann-MIT, and the Rosa and Emilio Segré Research Award. DP is thankful to the DART mission investigation team for fruitful collaboration. N.L.S. is funded by the Deutsche Forschungsgemeinschaft (DFG, German Research Foundation) via the Walter Benjamin program – 461903330.

DATA AVAILABILITY

The data presented in this paper is available in the electronic tables, while the code is accessible via GitHub³.

³ <https://github.com/EranOfek/AstroPack>

Property	Limits
$v_{\text{ej,fast}}$	$\approx 1600 \pm 200 \text{ m s}^{-1}$ [M]; with tail down to 500 m s^{-1} [LC]
$m_{\text{ej,fast}}$	$\gtrsim 1 \times 10^4 \text{ kg}$ [KE]
$r_{\text{p,fast}}$	$\gtrsim 0.2 \mu\text{m}$ [SP]; $\lesssim \text{few } \mu\text{m}$ [SM]
κ_{visible}	$\gtrsim 10^4$ [SP]
κ_{UV}	$\gtrsim 10^4$ [SP]
$v_{\text{ej,slow}}$	$\sim 0.1\text{--}10 \text{ m s}^{-1}$ [LC+M]
$m_{\text{ej,slow}}$	$\gtrsim 2 \times 10^5 Q_{\text{scat,slow}}^{-1} \text{ kg}$ [A+SM]; $\gtrsim 9 \times 10^5 \text{ kg}$ (with Q)
$r_{\text{p,slow}}$	$\gtrsim 1 \text{ mm}$ [A]; $\lesssim 14 \text{ m}$ [IS]; $\lesssim 3 \text{ m}$ [IS] (with Q)
$Q_{\text{scat,slow}}(\theta)$	$\gtrsim 0.07$ [SM, SP, LC]
$v_{\text{ej,tail}}$	$\lesssim 0.1 \text{ m s}^{-1}$ [A]
$m_{\text{ej,tail}}$	$\sim 800 Q_{\text{scat,tail}}^{-1}(\theta) \text{ kg}$ [A]
$Q_{\text{scat,tail}}$	$\sim 10^{-3}$ [SP]
$r_{\text{p,tail}}$	$\gtrsim 7 \mu\text{m}$ [A]; $\lesssim 1000 \mu\text{m}$ [A]

Table 6. Summary of estimated ejecta components and properties. For each limit, we also provide the method by which it was obtained: LC - light curve; KE - energy conservation; M - Motion in images; SM - surface area to mass; SP - scattering properties; T - Optical thickness; A - Acceleration due to radiation pressure; IS - Smoothness in images. See the text for details.

APPENDIX A: DERIVATION OF THE OPTICAL-THICKNESS TIME SCALE

Here, we develop a simple optical-thickness model, taking into account some of the geometrical properties of the DART impact. The observed flux in some band x is given by

$$f_x = f_{\odot,x} \Delta\Omega_p \mathbb{P}, \quad (\text{A1})$$

where $f_{\odot,x}$ is the flux from the Sun reaching the ejecta, $\Delta\Omega_p$ is the solid angle occupied by the ejecta, as seen by the observer, and \mathbb{P} is the probability that a photon that reaches the ejecta will be scattered into this solid angle. It is convenient to define the effective trajectory length of a photon within the ejecta, l_{eff} though

$$\mathbb{P} \equiv \frac{1}{\sigma_T} \frac{d\sigma}{d\Omega} \frac{l_{\text{eff}}}{l}, \quad (\text{A2})$$

where σ_T is the total (scattering plus absorption) cross-section, and l is the photon mean free path. In the limit that the ejecta is optically thick, we have $l_{\text{eff}} \approx l$, and in the limit that the ejecta is optically thin, we have $l_{\text{eff}} \approx L$, where L is the size of the ejecta. Before we derive a more realistic model, we would like to give some intuition regarding the asymptotic behavior of the flux, and this will be done by assuming some simple box-like geometry (that will be relaxed later on). In this case, we can write

$$\frac{f_x}{f_{\odot,x}} = \frac{1}{\sigma_T} \frac{d\sigma}{d\Omega} \frac{l_{\text{eff}}}{l} \Delta\Omega_p \quad (\text{A3})$$

$$= \begin{cases} \frac{1}{\sigma_T} \frac{d\sigma}{d\Omega} \Delta\Omega_p = \frac{1}{\sigma_T} \frac{d\sigma}{d\Omega} \frac{A_p}{\Delta^2} \propto t^2 & t \rightarrow 0, \\ nL \frac{d\sigma}{d\Omega} \Delta\Omega_p = N_p \frac{d\sigma}{d\Omega} \frac{1}{\Delta^2} = \text{const.} & t \rightarrow \infty, \end{cases} \quad (\text{A4})$$

where Δ is the observer-ejecta distance, and we used $\Delta\Omega_p = A_p/\Delta^2$, $A_p = L^2$ is the geometric area of the ejecta, $N_p = nL^3$ is the number of particles in the ejecta, and n is the particle density in the ejecta. Here, the $t \rightarrow \infty$ case is provided just to show that the flux goes into a constant value. Below, we are using a more realistic geometrical model.

To estimate l_{eff} , we require a geometrical model for the ejecta. The fast ejecta of the DART impact looks like a spherical section, with a half-opening angle $\gamma \approx 1$, width/radius $\delta \approx 0.5$ and a radial velocity v_{ej} . The maximal cylindrical radius of the shell is $w_2 = v_{\text{ej}} t \sin(\gamma)$ and we define the thickness of the spherical shell by $w_1 = \delta v_{\text{ej}} t$. Since the DART impact vector was roughly at $\alpha_{\text{DAO}} \approx 90$ deg from our line of sight and the Sun-Didymos-Earth angle $\theta = 53.3$ deg, we use the approximation in which the Sun shines in parallel with the section axis, and photons have to get out, to Earth, of the vertical direction. This approximation holds for $\delta \gtrsim |\alpha_{\text{DAO}} - \pi/2| \approx 0.1$ (here α_{DAO} and δ are in radians). Our approximation requires that $\sigma_{\text{abs}} \gg \sigma_{\text{scat}}$, which is consistent with the observations, as our analysis shows. This requirement means that each photon is scattered not more than one time.

Next, we define a cylindrical coordinate system in which we do the calculations, where z is the cylinder axis, r is the cylinder radius coordinate, and ϕ is the cylinder angle coordinate. We can write

$$l_{\text{eff}} = \frac{1}{\pi w_2^2} \int_0^{2\pi} \int_0^{w_2} \int_{z_1(r)}^{z_2(r)} e^{-\frac{z-z_1(r)}{l}} e^{-\frac{d(z,r,\phi)}{l}} r dr dz d\phi, \quad (\text{A5})$$

where the first term of the integrand is the probability to scatter within the ejecta (as the photon is moving along the z direction and the ejecta spans the region $[z_1(r), z_2(r)]$), and the second term of the integrand is the probability that the scattered photon will not suffer more scattering within the ejecta, where $d(z, r, \phi)$ is the distance the scattered photon has to travel within the ejecta. It is more convenient to use the outer radius of the shell $R_2 = w_2/\sin(\gamma)$ and the inner radius of the shell $R_1 = R_2 - w_1$ for the calculation. We obtain

$$z_1(r) = R_2 \left(1 - \sqrt{1 - \left(\frac{r}{R_2}\right)^2} \right), \quad (\text{A6})$$

$$z_2(r) - z_1(r) = \begin{cases} R_2 \left(\sqrt{1 - \left(\frac{r}{R_2}\right)^2} - \frac{r}{R_2} \cot(\gamma) \right) - R_1 \left(\sqrt{1 - \left(\frac{r}{R_1}\right)^2} - \frac{r}{R_1} \cot(\gamma) \right) & r \leq \Delta r, \\ R_2 \left(\sqrt{1 - \left(\frac{r}{R_2}\right)^2} - \frac{r}{R_2} \cot(\gamma) \right) & r > \Delta r, \end{cases} \quad (\text{A7})$$

where $\Delta r = R_1 \sin(\gamma)$ is the maximal cylindrical radius of the inner shell. To calculate d , we assume that the scattering event was at (z, r, ϕ) and assume Earth is along the x -axis (perpendicular to the z axis). Then, the distance to Earth within the ejecta is given by

$$d(z, r, \phi) = \begin{cases} \sqrt{\tilde{r}^2 - r^2 \cos^2(\phi)} - r \sin(\phi) & z \leq w_1, \\ \sqrt{\tilde{r}^2 - r^2 \cos^2(\phi)} - r \sin(\phi) - 2R_2 \sqrt{\left(\frac{R_1}{R_2}\right)^2 - \left(1 - \frac{z}{R_2}\right)^2} & z > w_1, \end{cases} \quad (\text{A8})$$

where

$$\tilde{r}(z) = \begin{cases} R_2 \sqrt{1 - \left(1 - \frac{z}{R_2}\right)^2} & z \leq R_2(1 - \cos(\gamma)), \\ R_2 \left(1 - \frac{z}{R_2}\right) \tan(\gamma) & z > R_2(1 - \cos(\gamma)), \end{cases} \quad (\text{A9})$$

is the maximal cylindrical radius at z .

The volume of the shell is given by

$$V = \frac{2}{3} \pi v_{\text{ej}}^3 t^3 (1 - \cos \gamma) (1 - (1 - \delta)^3). \quad (\text{A10})$$

For mono-size particles, the number density is:

$$n = \frac{9}{8\pi^2} \frac{M_{\text{ej}}}{\rho r_{\text{p}}^3 v_{\text{ej}}^3 t^3 [1 - \cos(\gamma)][1 - (1 - \delta)^3]}, \quad (\text{A11})$$

allowing us to write

$$\frac{R_2}{l} = \left(\frac{t_0}{t}\right)^2 \frac{1}{1 - (1 - \delta)^3}, \quad (\text{A12})$$

$$\frac{R_1}{l} = \left(\frac{t_0}{t}\right)^2 \frac{1 - \delta}{1 - (1 - \delta)^3}, \quad (\text{A13})$$

with

$$t_0 = \sqrt{\frac{9m_{\text{ej}}\sigma_{\text{T}}}{8\pi^2 \rho r_{\text{p}}^3 v_{\text{ej}}^2 (1 - \cos(\gamma))}}. \quad (\text{A14})$$

The value of l_{eff} can be calculated numerically as a function of t/t_0 (for a choice of γ and δ), allowing us to plot $f_x/f_{x,\infty}$, where $f_{x,\infty}$ is the observed flux at $t \rightarrow \infty$, in Figure A1.

For resonance scattering, this model assumes that the absorption cross-section for light entering the ejecta, and going out is roughly the same.

A1 Equations for particles with size distribution

So far we have written the equations for mono-size particles. For particles with differential size distribution dn/dr , we can use the following equations:

$$n = \frac{1}{V} \frac{M}{\frac{4}{3}\pi\rho} \int \frac{dn}{dr} r^3 dr, \quad (\text{A15})$$

and in this case, the effective absorption cross-section is

$$\sigma_{\text{abs}} = \int \frac{dn}{dr} \sigma_{\text{abs}}(r) dr, \quad (\text{A16})$$

while t_0 is given by:

$$t_0^2 = \frac{9m_{\text{ej}}}{8\pi^2 \rho v_{\text{ej}}^2 (1 - \cos \gamma)} \int \frac{dn}{dr} r^3 dr \int \frac{dn}{dr} \sigma_{\text{abs}}(r) dr. \quad (\text{A17})$$

A2 The model surface brightness

We next calculate the surface brightness for this geometrical model. We need to consider the range $0 \leq z \leq R_2 - R_1 \cos(\gamma)$ and $0 \leq h \leq \tilde{r}(z)$, where z is the distance from the edge of the ejecta closest to the Sun and h is the distance from the section axis. At early times, when the ejecta is not resolved, we can only measure the mean surface brightness by

$$I_x = \frac{f_x}{\Delta\Omega_p} = \Delta^2 \frac{f_x}{A_p}, \quad (\text{A18})$$

where A_p is given in our model by

$$A_p = 2 \int_0^{R_2 - R_1 \cos(\gamma)} \tilde{r}(z) dz \equiv R_2^2 f_S(\gamma, \delta) = v_{\text{ej}}^2 t^2 f_S(\gamma, \delta), \quad (\text{A19})$$

where f_S is some numerical factor (≈ 0.89 for $\gamma = 1$ and $\delta = 0.5$). At late times, when the ejecta is resolved, we may measure the surface brightness as a function of angular location within the ejecta, given by:

$$I_x(h, z) = A \begin{cases} \int_0^{x_1} e^{-\frac{z-z_1(r(x,h))}{l}} e^{-x/l} dx + \int_{x_2}^{2\sqrt{\tilde{r}(z)^2 - h^2}} e^{-\frac{z-z_1(r(x,h))}{l}} e^{-\frac{x-x_2+x_1}{l}} dx & z > w_1 \text{ and } h < \tilde{r}_1, \\ \int_0^{2\sqrt{\tilde{r}(z)^2 - h^2}} e^{-\frac{z-z_1(r(x,h))}{l}} e^{-\frac{x}{l}} dx & \text{otherwise,} \end{cases} \quad (\text{A20})$$

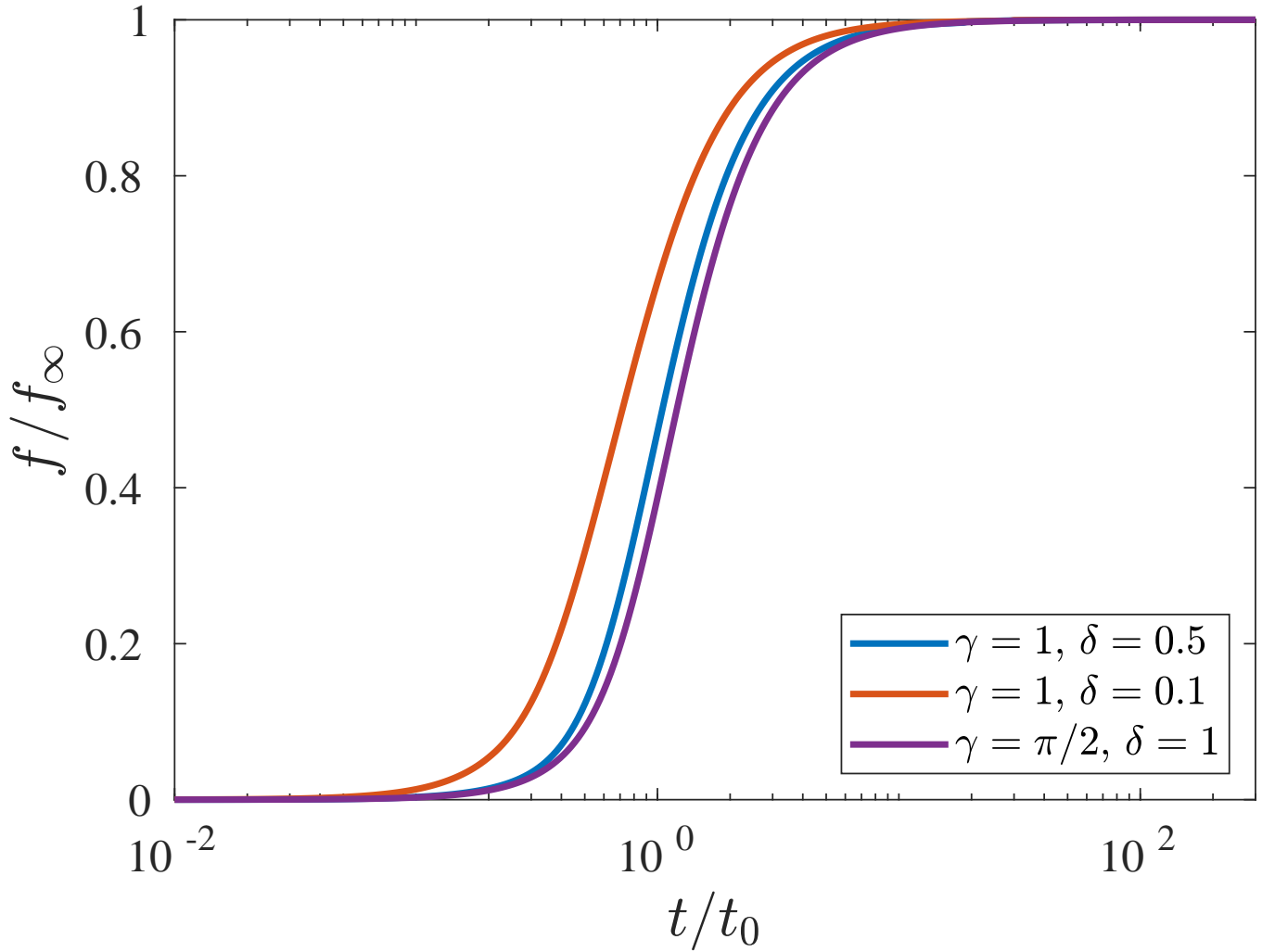


Figure A1. The theoretical rising light curve due to optical thickness model for selected values of γ and δ .

where x is the distance along the ejecta as seen from Earth, related to r through

$$r = \sqrt{\tilde{r}^2 + x^2 - 2x\sqrt{\tilde{r}^2 - h^2}}, \quad (\text{A21})$$

x_1 and x_2 are the coordinates of the inner shell, given by

$$x_1 = \sqrt{\tilde{r}^2 - h^2} - \sqrt{\tilde{r}_1^2 - h^2}, \quad (\text{A22})$$

$$x_2 = \sqrt{\tilde{r}^2 - h^2} + \sqrt{\tilde{r}_1^2 - h^2}, \quad (\text{A23})$$

and \tilde{r}_1 is the maximal cylindrical radius of the inner shell:

$$\tilde{r}_1(z) = R_2 \sqrt{\left(\frac{R_1}{R_2}\right)^2 - \left(1 - \frac{z}{R_2}\right)^2}. \quad (\text{A24})$$

To determine the constant A we note that for $t \rightarrow 0$ the surface brightness approaches the constant value, $f_{\odot,x}\sigma_{\text{T}}^{-1}d\sigma/d\Omega$, obtained at $h = z = 0$. From Equation (A20) we find for $t \rightarrow 0$ that $I_x(0,0) \rightarrow \int_0^{2\tilde{r}} e^{-x/l} dx \approx l$, such that

$$A = f_{\odot,x} \frac{1}{l\sigma_{\text{T}}} \frac{d\sigma}{d\Omega}. \quad (\text{A25})$$

The maximal surface brightness at any time is obtained at $h = 0$. The surface brightness at $h = 0$ is given in the limit $t \rightarrow \infty$, as

$$I_x(0,z) = 2f_{\odot,x} \frac{1}{l\sigma_{\text{T}}} \frac{d\sigma}{d\Omega} \begin{cases} \tilde{r} - \tilde{r}_1 & z > w_1, \\ \tilde{r} & z \leq w_1, \end{cases} \quad (\text{A26})$$

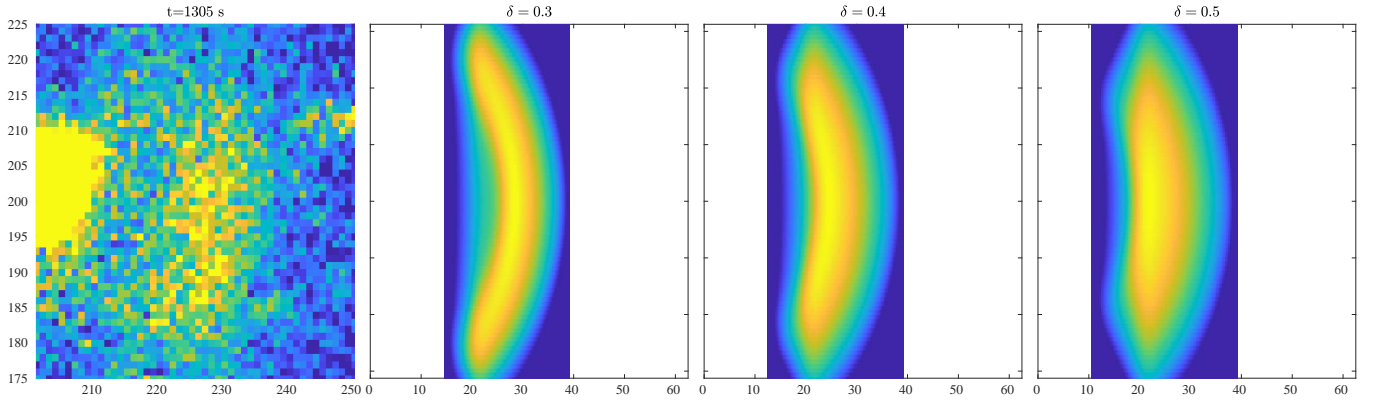


Figure A2. Didymos coadded image taken at $t = 1305$ s compared with the expected 2D surface brightness of a uniform density spherical cup model with $\gamma = 1$ and δ of 0.3, 0.4, and 0.5.

and the maximum of this function is given by

$$I_{x,\max} = 2f_{\odot,x} \frac{1}{\sigma_T} \frac{d\sigma}{d\Omega} \frac{R_2}{l} \begin{cases} \sqrt{1 - (1 - \delta)^2} & 1 - \delta > \cos(\gamma), \\ \sin(\gamma) & 1 - \delta \leq \cos(\gamma), \end{cases} \quad (\text{A27})$$

which can be written as

$$I_{x,\max} = 2f_{\odot,x} \frac{1}{\sigma_T} \frac{d\sigma}{d\Omega} \left(\frac{t_0}{t}\right)^2 \frac{1}{1 - (1 - \delta)^3} \begin{cases} \sqrt{1 - (1 - \delta)^2} & 1 - \delta > \cos(\gamma), \\ \sin(\gamma) & 1 - \delta \leq \cos(\gamma). \end{cases} \quad (\text{A28})$$

The ratio between $I_{x,\max}$ and I_x in the optically thin limit is given by:

$$\frac{I_{x,\max}}{I_x} = \frac{2}{1 - (1 - \delta)^3} \begin{cases} \sqrt{1 - (1 - \delta)^2} & 1 - \delta > \cos(\gamma), \\ \sin(\gamma) & 1 - \delta \leq \cos(\gamma). \end{cases} \quad (\text{A29})$$

For $\gamma = 1$ and $\delta = 0.5$, this ratio equal to 1.92.

Figure A2 shows the fast ejecta coadded image taken at $t = 1305$ s compared with our surface brightness model for a uniform density spherical cup model with $\gamma = 1$ and δ of 0.3, 0.4, and 0.5. $\gamma = 1$ and $\delta = 0.5$ provide a reasonable match to the data.

APPENDIX B: MIE SCATTERING INTERPRETATION

Prior to the realization that the light from the fast ejecta is due to emission lines from neutral gas, we attempted an interpretation based on the assumption that the fast ejecta is composed of scattering particles only. This analysis found out that the particles must be small (below a few microns) and that Mie-scattering is the relevant scattering process. The observations of [Shestakova et al. 2023](#) clearly show that the light of the fast ejecta is from resonance scattering of neutral atoms, and therefore, Mie scattering is not relevant (at least not for the majority of the observed light from the fast ejecta). Here we give a brief version of this analysis because we believe it is useful due to the following reasons: (i) This analysis shows, irrespective of the [Shestakova et al. \(2023\)](#) observations, that the particles in the fast ejecta must be smaller than $0.2 \mu\text{m}$, and that the mass of the fast ejecta must be dominated by particles smaller than $0.02 \mu\text{m}$. (ii) This line of analysis may be useful in the future for analyzing infrared spectra of tails.

The mass of the fast ejecta, $m_{\text{ej,fast}}$, can be constrained from energy conservation, $m_{\text{ej,fast}} v_{\text{ej,fast}}^2 \lesssim m_{\text{imp}} v_{\text{imp}}^2$, leading to $m_{\text{ej,fast}} \lesssim 10^4$ kg. Here the impactor mass is $m_{\text{imp}} \cong 579.4$ kg, and impact velocity $v_{\text{imp}} \cong 6145 \text{ m s}^{-1}$ ([Cheng et al. 2023](#)). The upper limit on the mass, along with the measured effective surface area of the ejecta gives us an upper limit on the typical particle radius, $r_p \lesssim 3m_{\text{ej}}/(4\rho S_{\text{eff}}) \sim 400 \mu\text{m}$ (for a 100% geometric scattering efficiency). For the fast ejecta we assume $\rho = 1500 \text{ kg m}^{-3}$ (Similar to regolith [McKay et al. 1972](#)).

For clarity, we first use a highly simplified description of the expanding fast ejecta: A spherical cloud expanding at $v_{\text{ej,fast}}$, composed of spherical particles with a dielectric constant of $n + i\kappa \approx 1.5 + 0.3i$ (i.e., silica dust; [Draine & Lee 1984](#)) and two discrete radii. This is because, as we show below, the scattering and absorption of light must be dominated by particles of different sizes. Later on, we present a more elaborate model, where the geometry is of an expanding shell consistent with the resolved images, the particle size distribution is continuous, and the dielectric constant is considered a free parameter. The key results obtained using this model and analysis are similar to those obtained using the simplified analysis.

The similarity of the maximal effective areas in the blue and UV bands, $S_{\text{eff,fast,B}} \approx 0.0125 \text{ km}^2$ and $S_{\text{eff,fast,UVW2}} \sim 0.014 \text{ km}^2$, and much smaller effective area at near-infrared, $S_{\text{eff,fast,z}} \lesssim 0.002 \text{ km}^2$, implies that the size of the particles dominating the scattering is similar to the B -band radiation wavelength – for particles with much larger radii the effective area would be similar at all wavelengths, while for particles with much smaller radii, the effective area in the blue and UV bands

would be significantly different. This is demonstrated in Figure B1 that shows that the radius of particles dominating the Mie scattering is $r_{p,\text{scat}} \approx 0.1 \mu\text{m}$.

When the cloud is optically thin the effective area of the scattering particles is $N_{\text{scat}} d\sigma/d\Omega(\theta)$, where N_{scat} is the number of scattering particles and $d\sigma/d\Omega(\theta)$ is their differential cross section for scattering in our direction ($\theta = 53.3 \text{ deg}$). Using $d\sigma/d\Omega \approx 0.02(\pi r_p^2)$ (see Figure B1) we find $N_{\text{scat}} \sim 2 \times 10^{19}$, and a total mass of the scattering particles of $M_{\text{scat}} \sim 150 \text{ kg}$.

Had the debris cloud been composed only of the $r_{p,\text{scat}} \approx 0.1 \mu\text{m}$ scattering particles dominating the scattering, it would have become optically thin when $n_{\text{scat}} \sigma_{\text{abs,scat}} L \approx 1$, where the ejecta length scale is $L \approx v_{\text{ej,fast}} t_{0,\text{scat}}$, the particle number density is $n_{\text{scat}} \approx N_{\text{scat}}/(4\pi L^3/3)$, $t_{0,\text{scat}}$ is the t_0 of the scattering particles, and $\sigma_{\text{abs,scat}} = \pi r_{p,\text{scat}}^2$ (the absorption cross section is similar to the geometric cross section for $2\pi r_p \gtrsim \lambda$; see Figure B1), yielding $t_{0,\text{scat}} \approx 0.2 \text{ s}$ (see Fig. 5). The observed value of $t_{0,\text{fast}}$, which is an order of magnitude larger than $t_{0,\text{scat}}$, implies that the effective absorption cross-section per scattering particle should be two orders of magnitude larger than the scattering particles' geometric cross-section, $\sigma_{\text{abs,eff.}} \approx 10^2 \pi r_{p,\text{scat}}^2$. This implies that the cloud contains a mass $M_{\text{abs}} \sim 10^2 M_{\text{scat}}$ of particles of size $r_{p,\text{abs}} \ll r_{p,\text{scat}}$, that dominates the absorption and do not contribute significantly to the scattering.

Small particles, $r_{p,\text{abs}} \ll r_{p,\text{scat}} \approx \lambda$, may dominate the absorption while contributing little to the scattering since their absorption cross section is suppressed compared to their geometric cross section by a factor of $r_{p,\text{abs}}/\lambda$ (Figure B1), while their scattering cross section is suppressed by a factor of $(r_{p,\text{abs}}/\lambda)^2$. The total contribution of such particles to the absorption is independent of their size and depends only on their total mass, since the number of particles is $\propto M_{\text{abs}}/r_{p,\text{abs}}^3$ while their absorption cross section is $\approx \pi r_{p,\text{abs}}^2 (r_{p,\text{abs}}/\lambda) \propto r_{p,\text{abs}}^3$. The observed $\sigma_{\text{abs,eff.}} \approx 10^2 \pi r_{p,\text{scat}}^2$ therefore implies $M_{\text{abs}} \sim 10^2 M_{\text{scat}} \sim 1.5 \times 10^4 \text{ kg}$, which is of the order of magnitude of the upper limit on the fast ejecta mass. Assuming a factor of about 3 uncertainty on the measurement of $d\sigma/d\Omega/\sigma_{\text{T}}$ this is translated to about $m_{\text{ej,fast}} \gtrsim 5000 \text{ kg}$. In this case, the mass of the fast ejecta is close to the maximum allowed by energy conservation, $\approx 10^4 \text{ kg}$, and most of this mass is composed of small particles, with $r_{p,\text{abs}} \ll 0.1 \mu\text{m}$, and that $\sim 10^2 \text{ kg}$ of the mass is carried by particles with $r_{p,\text{scat}} \approx 0.1 \mu\text{m}$ that dominate the scattering.

We fitted a simple Mie-scattering model⁴ to the observational constraints. Our model includes spherical particles with refractive index $n + i\kappa$ which is wavelength-independent, reflecting Sun light at angle $\theta = 53.3 \text{ deg}$. The particles follow a differential size distribution of the form

$$\frac{dN}{dr} \propto r^{-\alpha}, \tag{B1}$$

where α is the power law index of the size distribution, between minimum and maximum radii R_{min} and R_{max} , respectively. We use our geometrical model (§A1) with $\gamma = 1$ and $\delta = 0.5$. The observational constraints include:

- (1) $m_{\text{ej,fast}} < 10^4 \text{ kg}$;
- (2) $S_{\text{eff,fast,B}} = 0.0125 \text{ km}^2$;
- (3) $0.33 < Q_{\text{scat,UVW2}}/Q_{\text{scat,B}} < 3$;
- (4) $Q_{\text{scat,B}}/Q_{\text{scat,z}} > 4$;
- (5) $8.5 \times 10^{-5} < d\sigma/\Omega(\theta)/\sigma_{\text{T}} < 1.05 \times 10^{-3} \text{ sr}^{-1}$.

Our model assumes $\theta = 53.3 \text{ deg}$ and $\sigma_{\text{T}} \gg \sigma_{\text{scat}}$, where σ_{scat} is the total scattering cross-section of the particle. Given all these assumptions and additional uncertainty in the value of the observed parameters, we adopted a wide range for the observed parameters. In all cases, we assumed $\rho = 1500 \text{ kg m}^{-3}$ (McKay et al. 1972). We scanned over the following parameters: (i) n in the range of 1.05 to 2.5 in steps of 0.025. (ii) κ in the range of 0.01 to 1 with 25 logarithmic steps. (iii) R_{min} in the range of 0.01 to $0.1 \mu\text{m}$ in 12 logarithmic steps. (iv) R_{max} in the range of 0.1 to $0.6 \mu\text{m}$ in 20 logarithmic steps, and (v) α in the range of 1.6 to 6 with step of 0.2.

This model constrains some of the parameters very well. For example, larger R_{max} will make the z band reflectance higher and will violate the observations. This requires $R_{\text{max}} \approx 0.2 \mu\text{m}$. $\alpha \approx 4.6$ is required in order to satisfy the observations. Most importantly, based on this simple model, the mass of the fast ejecta needs to be close to the upper limit on the fast ejecta mass (from energy conservation), and we find $m_{\text{ej,fast}} \sim 9000 \text{ kg}$. Given the Shestakova et al. (2023) observations, this estimate is not valid. However, the limits on the particle sizes are still valid, and they are independent of the emission lines observation.

REFERENCES

- A'Hearn M. F., et al., 2005, *Science*, **310**, 258
 Ben-Ami S., et al., 2023, *arXiv e-prints*, p. arXiv:2304.02719
 Britt D. T., Consolmagno G. J., 2003, *M&PS*, **38**, 1161
 Brosch N., Kaspi S., Niv S., Manulis I., 2015, *APSS*, **359**, 9
 Cheng A. F., et al., 2018, *P&SS*, **157**, 104
 Cheng A. F., et al., 2023, *Nature*
 Daly R. T., et al., 2023, *Nature*
 Draine B. T., Lee H. M., 1984, *ApJ*, **285**, 89
 Fahnestock E. G., et al., 2022, *PSJ*, **3**, 206
 Farinella P., Davis D. R., 1992, *Icarus*, **97**, 111

⁴ <https://www.mathworks.com/matlabcentral/fileexchange/36831-matscat?requestedDomain=>

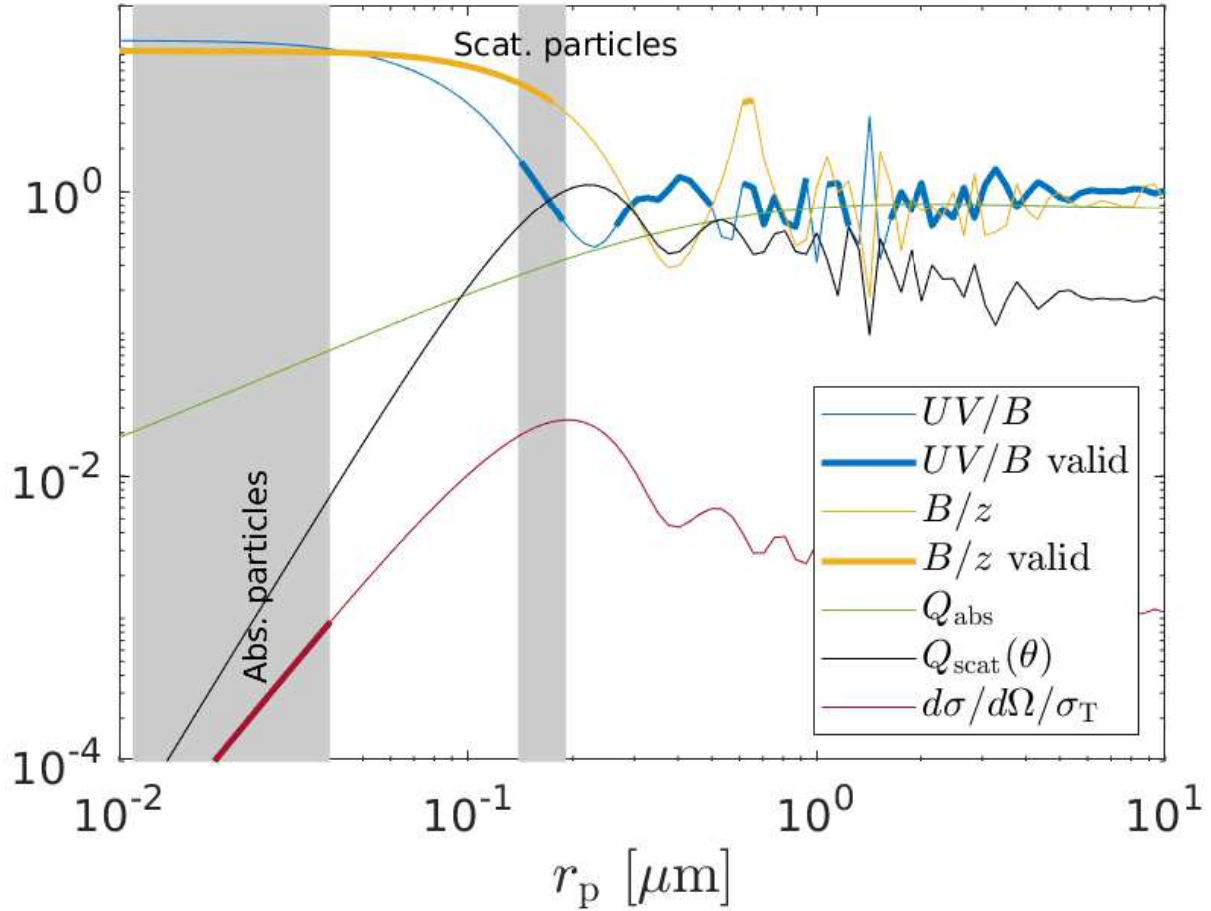


Figure B1. The Mie scattering properties as a function of particle radius for $n + i\kappa = 1.5 + i0.3$. The blue line represents the calculated $UVW2$ to B_p band ratio, while the yellow line is the same but for the B_p vs. z ratio. This calculation takes into account the spectral transmission as well as the solar spectrum in the band. The heavy lines (and gray patches) show the regions that satisfy the observational constraints. The green line shows the absorption efficiency (Q_{abs} ; absorption cross section divided by πr_p^2), while the black line is for the scattering efficiency ($Q_{\text{scat}}(\theta) = d\sigma/d\Omega(\theta)/(\pi r_p^2)$), multiplied by 100. The red line shows $d\sigma/d\Omega(\theta)/\sigma_T$.

Gehrels N., 1986, *ApJ*, 303, 336

Gehrels N., et al., 2004, *ApJ*, 611, 1005

Graykowski A., et al., 2023, *Nature*

Gudebski T., Heldridge E., McGawn B., Hill E. O., Swift J. J., Zhou H., 2023, *Research Notes of the American Astronomical Society*, 7, 178

Gustafson B. A. S., 1994, *Annual Review of Earth and Planetary Sciences*, 22, 553

Haisch B., Strong K. T., Rodono M., 1991, *ARA&A*, 29, 275

Harker D. E., Woodward C. E., Wooden D. H., 2005, *Science*, 310, 278

Holsapple K. A., 2022, *P&SS*, 219, 105529

Holsapple K. A., Housen K. R., 2019, *P&SS*, 179, 104724

Housen K. R., Schmidt R. M., Holsapple K. A., 1983, *J. Geophys. Res.*, 88, 2485

Ishiguro M., et al., 2011, *ApJ*, 740, L11

Jewitt D., Weaver H., Agarwal J., Mutchler M., Drahus M., 2010, *Nature*, 467, 817

Jewitt D., Weaver H., Mutchler M., Larson S., Agarwal J., 2011, *ApJ*, 733, L4

Jewitt D., Kim Y., Li J., Mutchler M., 2023, *ApJ*, 952, L12

Keller S. C., et al., 2007, *Publ. Astron. Soc. Australia*, 24, 1

Kim Y., Jewitt D., 2023, arXiv e-prints, p. arXiv:2309.15116

Kumamoto K. M., et al., 2022, arXiv e-prints, p. arXiv:2209.11876

Li J.-Y., et al., 2023, *Nature*

Lierle P., Schmidt C., Baumgardner J., Moore L., Lovett E., 2023, arXiv e-prints, p. arXiv:2307.16872

Luther R., Zhu M.-H., Collins G., Wunnemann K., 2018, *Meteorite & Plan. Sci.*, 53, 1705

McKay D. S., Heiken G. H., Taylor R. M., Clanton U. S., Morrison D. A., Ladle G. H., 1972, Lunar and Planetary Science Conference Proceedings, 3, 983

- Meech K. J., et al., 2005, *Science*, **310**, 265
- Moreno F., et al., 2011, *ApJ*, **738**, 130
- Moreno F., et al., 2023, *PSJ*, **4**, 138
- Ofek E. O., 2014, MATLAB package for astronomy and astrophysics (ascl:1407.005)
- Ofek E. O., 2019, *PASP*, **131**, 054504
- Ofek E. O. e. a., 2023, submitted.
- Ofek E. O., Ben-Ami S., 2020, arXiv e-prints, p. [arXiv:2011.04674](https://arxiv.org/abs/2011.04674)
- Rivkin A. S., et al., 2021, *PSJ*, **2**, 173
- Roming P. W. A., et al., 2005, *SSRv*, **120**, 95
- Roth N. X., et al., 2023, *arXiv e-prints*, p. [arXiv:2306.05908](https://arxiv.org/abs/2306.05908)
- Sánchez P., Scheeres D. J., Quillen A. C., 2022, arXiv e-prints, p. [arXiv:2209.11353](https://arxiv.org/abs/2209.11353)
- Shestakova L., Serebryanskiy A., Aimanova G., 2023, *Icarus*, **401**, 115595
- Soumagnac M. T., Ofek E. O., 2018, *PASP*, **130**, 075002
- Tancredi G., Liu P.-Y., Campo-Bagatin A., Moreno F., Domínguez B., 2022, arXiv e-prints, p. [arXiv:2209.02805](https://arxiv.org/abs/2209.02805)
- Thomas C. A., et al., 2023, *Nature*
- Wolf C., et al., 2018, *Publ. Astron. Soc. Australia*, **35**, e010
- Zackay B., Ofek E. O., 2017, *ApJ*, **836**, 187
- Zhang Q., Battams K., Ye Q., Knight M. M., Schmidt C. A., 2023, *PSJ*, **4**, 70

This paper has been typeset from a $\text{\TeX}/\text{\LaTeX}$ file prepared by the author.